4 Experiment

4.1 Experimental Chamber

The experimental chamber used for all synchrotron based experiments has two segments. The smaller section, the *preparation chamber* is equipped with a manipulator holding a filament for heating, a gate valve and a dosing valve for evaporation purposes and an ion gun for sample cleaning. A fast load lock can be used for easy sample exchange. The

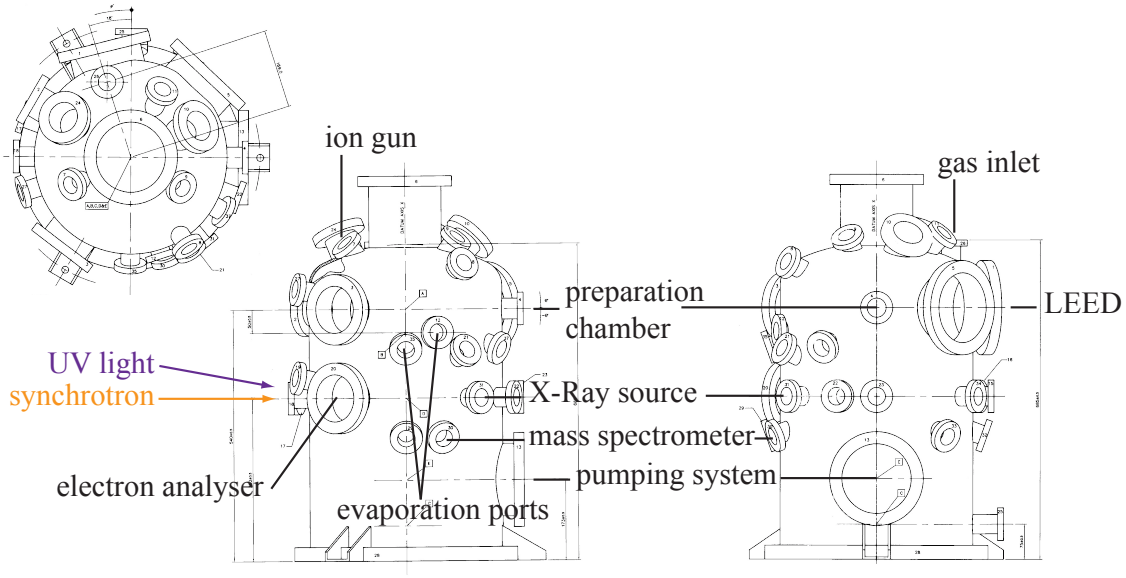

Figure 4.1: *Photos of the experimental chamber attached to the UE56/2-PGM1. The left photo shows the "front" of the chamber, i.e. the side on which the operator's desk is situated, the right image shows the "back" of the chamber.*

preparation chamber is connected to the *analysis chamber*. This segment is equipped with a manipulator which can be moved within five axes (x-, y-and z- movement, Θ angle rotation around the main axis and Φ angle rotation around the sample normal). The sample holder can be electrically isolated from the rest of the chamber to allow application of an extraction voltage for e-beam heating with the filament or direct current heating. Direct current heating is realized by contacting the sample with a wobble stick. For sample

cooling the manipulator has a central reservoir which can be filled with liquid nitrogen or helium. Copper braids connect the reservoir to the sample holder. The analysis chamber has two levels. The lower level is used for analysis, bearing the beamport, a sapphire-window for UV exposure and the electron analyser and an x-ray source. The electron analyser is a *SPECS Phoibos 100* hemispherical analyser with 2D-CCD-detector. The upper level is used for in-situ sample preparation holding two gate valves for insertion of evaporators, two dosing valves for gas inlets and an ion gun for bombardment. A LEED optics is installed on the upper level for sample analysis using electron diffraction.

The scanning tunneling microscopy experiments have been performed in a separate chamber also equipped with above mentioned sample preparation tools. A LEED optics for sample analysis was also attached. A SPECS variable temperature scanning tunneling microscope (VT-STM) was used.

4.2 Photoelectron Spectroscopy (XPS and UPS)

One of the main technique used in this work is photoelectron spectroscopy[24–26][1], which is shown in figure 4.2.

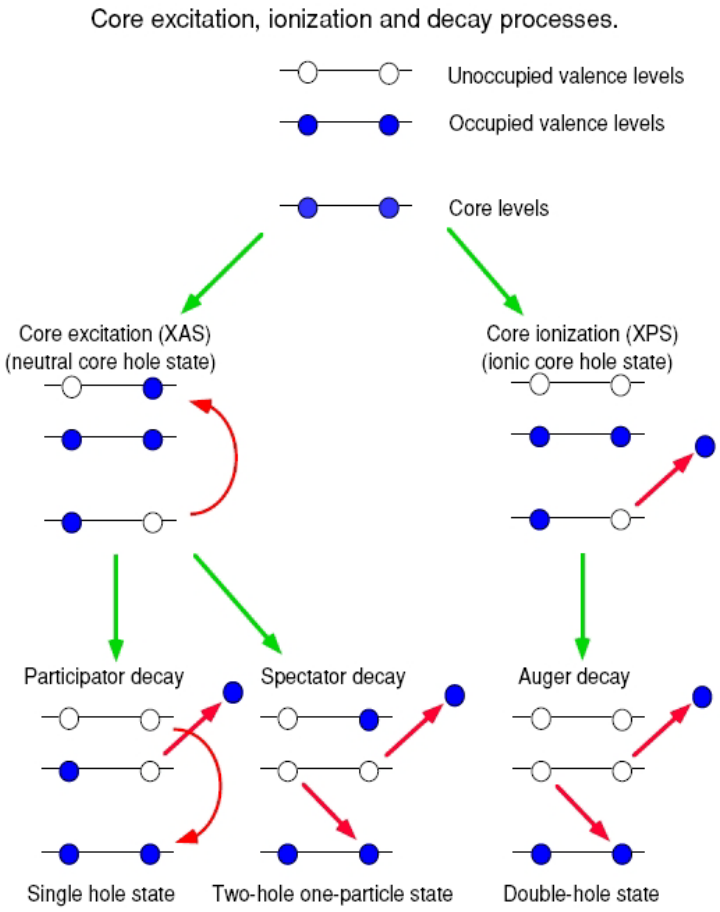

Figure 4.2: *Overview of possible photoexcitation processes[29] in a solid. Upon photoexcitation, electrons can either be excited into an unoccupied state (XAS, left) or ionized into the vacuum (XPS, right). Both processes will be utilized throughout this work. In photoemission, the kinetic energy of the ionized electron is detected. After ionization a core hole is left at the atom, which can be filled by an electron from a higher energy state. Simultaneously an Auger electron is emitted as well (which can also be detected). After core excitation, the appearing core hole can either be filled through back decay of the original electron, simultaneously emitting an electron from filled higher energy levels (participator decay) or through an Auger process (spectator decay). In both cases the finally emitted electron can be detected. – Figure reproduced from [29].*

Photoelectron spectra provide a good insight into the chemical environment of an atom and is often used as electron spectroscopy for chemical analysis (ESCA)[30], which is of-

[1] A good overview can be found in the book of Ertl[27], a detailed description is, for example, given by Fadley[28].

ten referred to as X-ray photoelectron spectroscopy (XPS), but also a picture of the band structure[31] of the material and gives thereby an insight into its electronic and conductive properties[32, 33], also referred to as UV light photoelectron spectroscopy (UPS). The investigation of electrons of low binding energy is usually named UPS (UV-light photoelectron spectroscopy). These electrons provide a picture of the band structure[31] of the material and thereby an insight into its electronic and conductive properties[33].

This spectroscopic technique is based on the excitation of an electron from within an N-electron system with light of the energy $E_{exc} = h\nu$ into an $(N-1)$ final state[29]. Initial and final state are described by a wavefunction $\Psi^i(N)$ and $\Psi^f(N-1,k)$ and an energy $E^i(N)$ and $E^f(N-1,k)$ for initial and final state, respectively. The value k labels the initial level of the removed electron. Energy conservation leads to the equation

$$E^i(N) + h\nu = E^f(N-1,k) + E_{kin} \ , \tag{4.1}$$

with E_{kin} the kinetic energy of the removed electron. In the simplest approximation, called "Koopmans' Theorem", the $N-1$ electrons remain unchanged in spatial arrangement and energy. Thus the binding energy with respect to the vacuum level $E_B^V(k)$ is just the negative energy of the removed electron

$$E_B^V(k) = -\epsilon_k \tag{4.2}$$

$$E_B^V(k) = E^f(N-1,k) - E^i(N) \tag{4.3}$$

With equation 4.1 one obtains

$$E_B^V(k) = E_{kin} - h\nu \ . \tag{4.4}$$

Upon escape from the sample, photoelectrons have to overcome the surface potential barrier, whose magnitude is given by the work function Φ. The work function is defined as the difference between the chemical potential of the sample and the potential immediately outside the sample, that is position independent[34]. The latter one is referenced to as "vacuum level" E_{vac}. The actual energy of this vacuum level depends on the actual nature of the surface. At $T = 0K$ the work function would be the minimum photon energy at which photoemission occurs. The chemical potential of the sample is often expressed in terms of the "Fermi level" E_F. In metal samples the Fermi level is normally located at $1/2\ kT$ in the onset of the valence band. For semiconductor or insulators, which present an occupied valence and an unoccupied conduction band separated by the energy gap E_g, E_F is located in the middle between both. The highest level of the valence band is the photoelectron threshold E_T, the lowest unoccupied level is determined by the electron affinity E_A. The same holds true for molecules, where the equivalents for valence and con-

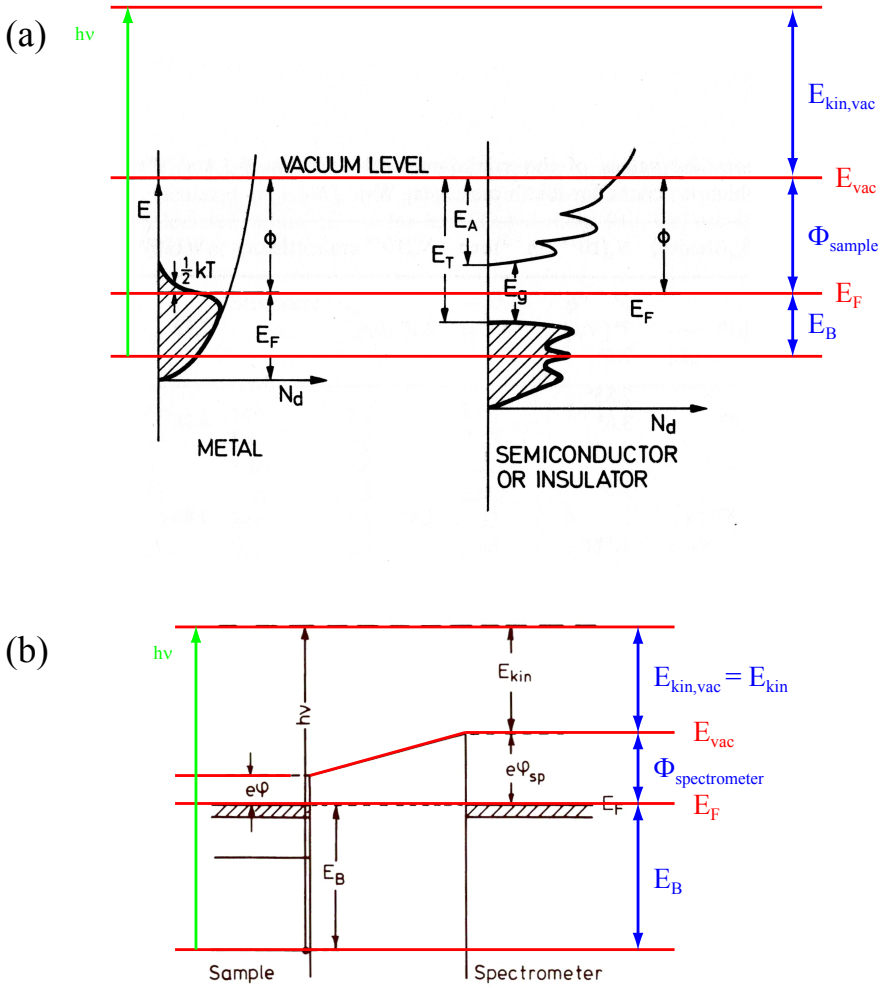

Figure 4.3: *On top (a) the energy level diagram for an XPS process[34] is depicted. The different definitions for the Fermi level in metals and semiconductors are shown. For clarity, the vacuum and Fermi level as well as kinetic energy, binding energy and workfunction have been emphasized. At the bottom (b) the Fermi level pinning of spectrometer and sample is shown. Thus the detected workfunction is the spectrometer workfunction[27]. Relevant levels and energies are again emphasized. – Figures reproduced from [34] and [27].*

duction band are given by the highest occupied molecular orbital (HOMO, at E_T) and the lowest unoccupied molecular orbital (LUMO, at E_A), respectively. This is schematically depicted at the top in figure 4.3. The kinetic energy detected is

$$E_{kin,vac} = h\nu - E_B - \phi_{sample} \ . \tag{4.5}$$

Since spectrometer and sample are electrically connected, their Fermi energies are aligned on the same level, and the spectrometer workfunctions determines the kinetic energy detected, as is shown at the bottom in figure 4.3. Thus the kinetic energy detected is

$$E_{kin,vac} = h\nu - E_B - \phi_{spectrometer} \ . \tag{4.6}$$

For simplification $E_{kin,vac}$ will from now on only be denoted as E_{kin}. In order to properly determine the electron binding energies E_B from the measured kinetic energies E_{kin}, the spectrometer work function $\phi = \phi_{spectrometer}$ has to be determined. Then all parameters from equation 4.6 are known:

$$E_{kin} = h\nu - E_B - \phi \ . \tag{4.7}$$

In this work this has been done using a clean Si(100) sample. The binding energy E_B for the bulk-peak is given as 99.20 eV[35], experimentally a binding energy of 103.25 eV has been determined without workfunction correction. Therefore the spectrometer workfunction equals $\phi = 4.05$ eV. Subsequently binding energies are corrected to this workfunction and are given with respect to the Fermi level.

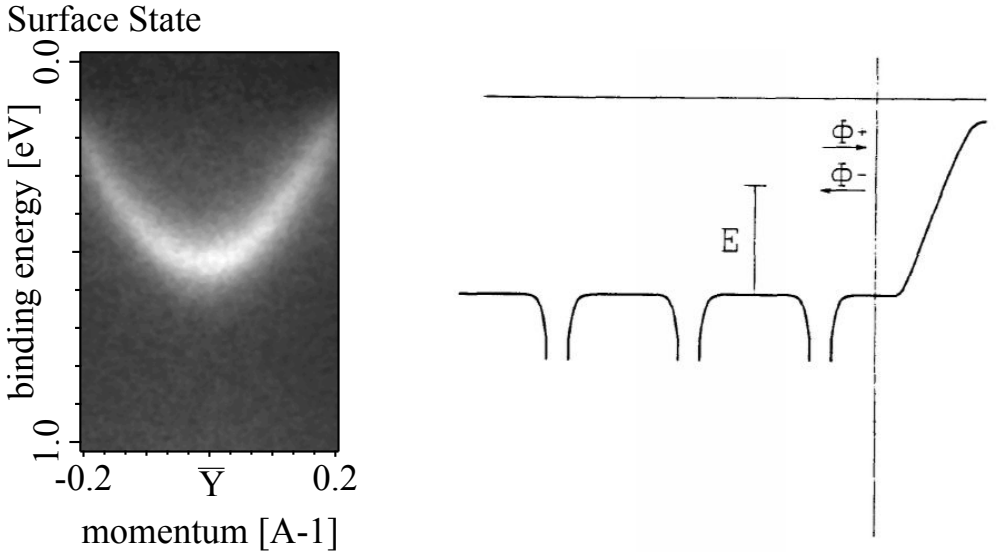

(a) *Surface state of Cu(110)* **(b)** *Potential model*

Figure 4.4: *(a) shows the surface state of a clean Cu(110) surface[36] at 0.5 eV binding energy[37]. In (b) a simple model of the potentials at a crystal surface is shown. Within the crystal a periodic potential exists while at the surface a potential barrier toward the vacuum exists. Electrons trapped there form the surface state[38]. – Figure reproduced from [38].*

A special manifestation of the surface potential barrier ϕ is the so called "surface state". The surface state is a spectral feature, that has widely been studied on a theoretical and experimental basis[37–44]. Accordingly a full theoretical description exists, allowing for a detailed analysis of the properties of surface states.

For the purpose here a simple model picture of surface states as shown in figure 4.4 is sufficient. The crystal lattice gives rise to a periodic Kronig-Penney potential[39, 40]. At

the surface, this periodicity is immediately lost. Instead a high potential barrier, responsible for the workfunction, exists, that hinders the immediate escape of electrons into the vacuum. In this simple picture the surface state is considered as a wave trapped between the bulk crystal and the surface barrier, where different constraints apply to the solution of the Schrödinger equation. The electrons in such state may not penetrate into the bulk when the solid shows a negative electron affinity, which is true for metals, and they do not have enough energy to escape into the vacuum, because of the potential created by the polarization charge the electrons induce at the surface, i.e. their image potential. Upon adsorption of molecules charge is transferred between substrate and adsorbate and the workfunction is altered. As this surface potential barrier is changed, the electrons may not be trapped any more. Therefore the alteration of the surface potential due to adsorption is directly manifested in the surface state.

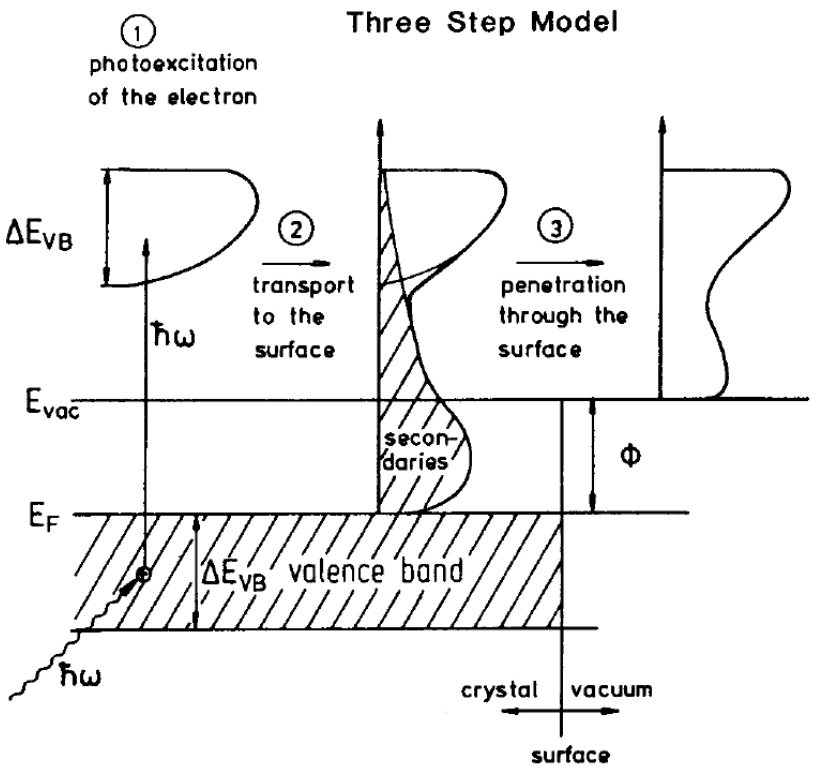

Figure 4.5: *Schematic representation of the three-step-model[45, 46]: (1) excitation of the electron (2) transport through the solid, (3) escape into the vacuum. – Figure reproduced from [47].*

Obviously the simple model used up to now to explain the photoemission process does not take into account the relaxation of the remaining electrons due to the presence of the hole. The most often used approximation is the so called *"sudden approximation"* stating that the excitation is very fast compared to the relaxation processes. This is well explained by the *"three-step model"* as proposed by Berglund and Spicer[45, 46] sketched in figure 4.5, which has proven to be a good approximation. In this model, the photoemission process

is divided into three steps

- excitation of the electron (I)
- transport through the solid (II)
- escape into the vacuum (III)

Throughout these steps the electrons may be affected by many phenomena[48]. These are inelastic scattering in the interior of the solid, energy losses owing to surface excitations, intrinsic energy losses induced by the electrons that screen the core hole and subsequent relaxation processes, elastic scattering of the electrons in the screened Coulomb field of the atomic cores, surface roughness, refraction of the signal electrons by the potential barrier at the surface, the experimental geometry and diffraction effects i.e. coherent scattering.

Consequently the energy distribution curve $I(E,\omega)$ of emitted photoelectrons is a sum of a primary distribution of undisturbed electrons $I_p(E,\omega)$, that escape from the sample without energy loss, and a secondary distribution of intrinsically scattered electrons $I_s(E,\omega)$[34]:

$$I(E,\omega) = I_p(E,\omega) + I_s(E,\omega) \ . \tag{4.8}$$

The primary distribution is factorized into three components, the distribution of photoexcited electrons ($P(E,\omega)$, step I), a transmission function ($T(E)$, step II) and an escape function ($D(E)$, step III).

$$I_s(E,\omega) = P(E,\omega) \times T(E) \times D(E) \ . \tag{4.9}$$

Since forward scattering processes play almost no role for the incoherent electron transfer in the solid[49], the inelastic scattering probability can be described by an isotropic mean free path $\lambda_e(E)$[45, 46]. Thus the transmission is

$$T(E) = \frac{\lambda_e(E)/\lambda_{ph}(\omega)}{1+\lambda_e(E)/\lambda_{ph}(\omega)} \ , \tag{4.10}$$

with $\lambda_{ph}(\omega)$ being the attenuation length of the exciting photons. The potential barrier at the surface is the Fermi energy E_F plus the sample workfunction Φ. Thus only electrons with an energy component perpendicular to the surface larger than $E_F + \Phi$ can escape from the surface. Assuming these electrons to be plane-wave-like with $E = k^2/2$[34], then the electrons can only escape in a cone with an angle θ off the surface normal, where

$$cos\theta = \left(\frac{E_F+\Phi}{E}\right)^{1/2} \ . \tag{4.11}$$

For an isotropic distribution of electrons inside the sample, the escape function is then

$$D(E) = \begin{cases} 1/2\,[1 - cos\theta] & E > E_F + \Phi \\ 0 & elsewhere \end{cases} . \quad (4.12)$$

Below the low energy cutoff both functions $T(E)$ and $D(E)$ are smooth functions of (E) and do not give rise to additional structures to $I_p(E, \omega)$. The distribution $P(E, \omega)$ is given by the photoexcitation of electrons from occupied states n into unoccupied states n' with the energies E_n and $E_{n'}$, respectively.

Under reasonable assumptions, e.g. conservation of the k-vector quantum number, the dielectric constant can be expressed like this:

$$J(\omega) = \frac{1}{(8\pi)^3} \sum_{n,n'} \int d^3k \delta[E_{n'}(k) - E_n(k) - \omega] \; . \quad (4.13)$$

This value J, named the joint density of states (JDOS), is just the total number of transitions possible at a photon energy ω.

Analogous the distribution $P(E, \omega)$ can be reduced to three terms, two energy surfaces and an integral representing a curve at the intersection of these two surfaces where $E_{n'} = E$ and $E_N = E - \omega$. This description gives rise to singularities. Therefore in the electron distribution curves for different photon energies, states can be observed that do change their position with photon energy and states that do not change their position. For the secondary distribution $I_s(E, \omega)$ Berglund and Spicer derived a function similar in derivation to $T(E)$. As multiple scattering is most likely to occur, this function will also be seemingly structureless[45, 46]. Eventually peaks due to plasmon losses might occur, but these will be energetically well separated from the primary signal and may thus be neglected here.

Evaluating the integral that defines the electron density of states gives

$$N(E) \propto \sum_n \int_{surface E_n(k)=0} \frac{dS}{|\nabla_k E_n(k)|} \; . \quad (4.14)$$

While for low energies a peak in $N(E)$ appears at positions where a transition into a defined final state E is possible, for higher energies the final state term becomes neglectably small and thus spectra have to be interpreted in a initial state picture.

The resulting spectrum contains a strong peak corresponding to “Koopmans’ Theorem”, as explained at the beginning of this chapter, with additional significant smaller peaks at higher binding energies.

As emitted electrons also undergo inelastic scattering within the spectrometer, an addi-

tional background is always present in the spectrum. This background can be removed using the function described by Shirley[50, 51].

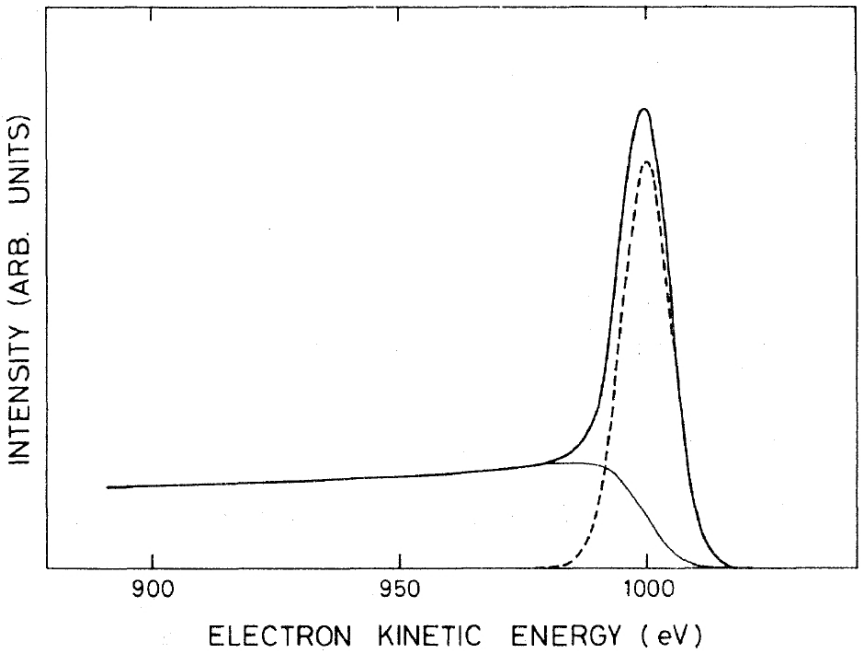

Figure 4.6: *Schematic representation of a PES spectrum with a gaussian type signal on a continuous background due to inelastically scattered electrons. Shown is the background spectrum calculated according to Shirleys method[50–52]. – Figure reproduced from [52].*

A Shirley background $S(E_B)$ was subtracted at binding energies E_B, where also photoemission signals were present in the spectrum, with the lower and upper binding energy limit E_{B1} and E_{B2} ($E_B1 > E_B2$), respectively. The corresponding intensities are denoted I_1 and I_2

$$S(E_B) = I_2 + \kappa \frac{A_2(E)}{A_1(E) + A_2(E)} \ , \tag{4.15}$$

where A_1 and A_2 are the areas under the graph between E_{B1} and E_B and, respectively, E_B and E_{B2}. This process was repeated until the resulting spectra were self-consistent, i.e. no further Shirley background could be defined. A typical Shirley background is depicted in figure 4.6.

As a complementary approach to this quite simple background Tougaard developed a more realistic formula to describe the background in photoelectron spectra[52, 53]. He divided the spectra in a near-peak and an off-peak-region. The near-peak region is dominated by electrons that may have lost energy but have not been substantially deflected, i.e. are emitted from near-surface regions. The dominating component in the off-peak region are highly angular deflected electrons at or close to their initial energy. Considering the

possible effects in each region Tougaard developed a set of formulas allowing for the back-calculation of the original spectrum from a measured one. Figure 4.7 shows a simulation of these.

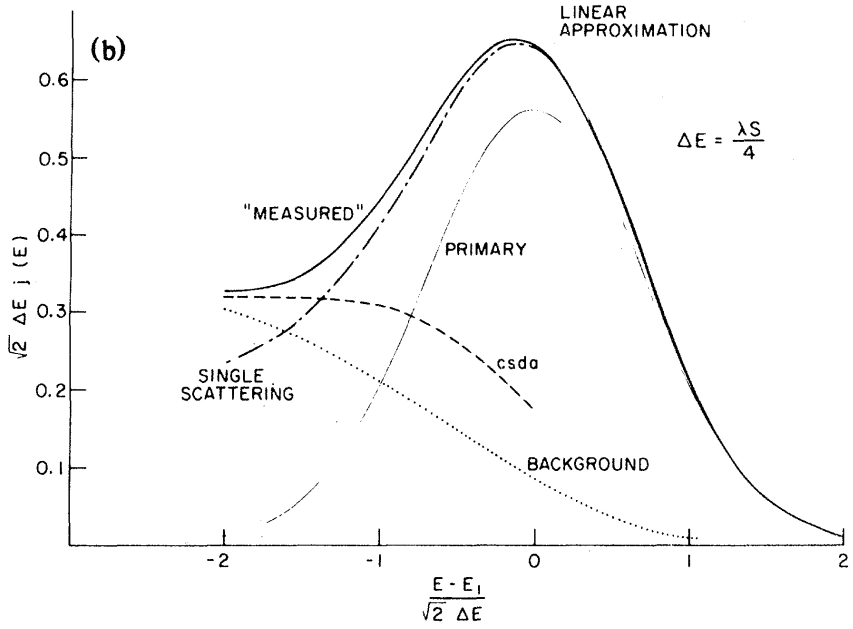

Figure 4.7: *Simulated spectrum from a primary gaussian emission[52]. The difference between "measured" and "primary" spectrum is given as background. Contributions from single scattering and the continuous slowing-down approximation (csda) are also given. For details see [52]. – Figure reproduced from [52].*

Still the Shirley method can be considered to supply reasonable results. Due to its simplicity it was used throughout this work.

The experiments have been performed at the synchrotron radiation facility *Berliner Elektronenspeicherring für Synchrotronstrahlung* (*BESSY*), mainly at the *Max-Planck-Beamline UE56/2-PGM1*[2], which is shown in figure 4.9, and partially also at the *PM3*-beamline (figure 4.10).

Synchrotron radiation is based on the emittance of light upon the "bending" of electrons moving with approximately the speed of light c. Upon this bending, e.g. in a bending magnet of an electron storage ring, light is emitted transversal to the circular electron path of the characteristic wavelength λ_c depending of the path radius and the bending magnet strength (see 4.8)[54, 57]. If several magnetic entities are coupled behind each other this process is of course multiplied. This is the underlying process of an undulator. The deflection at each magnet pair is kept small. Therefore the emission angle is small and the emission cones from every magnet pair can coherently overlap to form highly brilliant light with a high flux density.

[2]First experiments on trans-Stilbene have been performed at the UE56/2-PGM2.

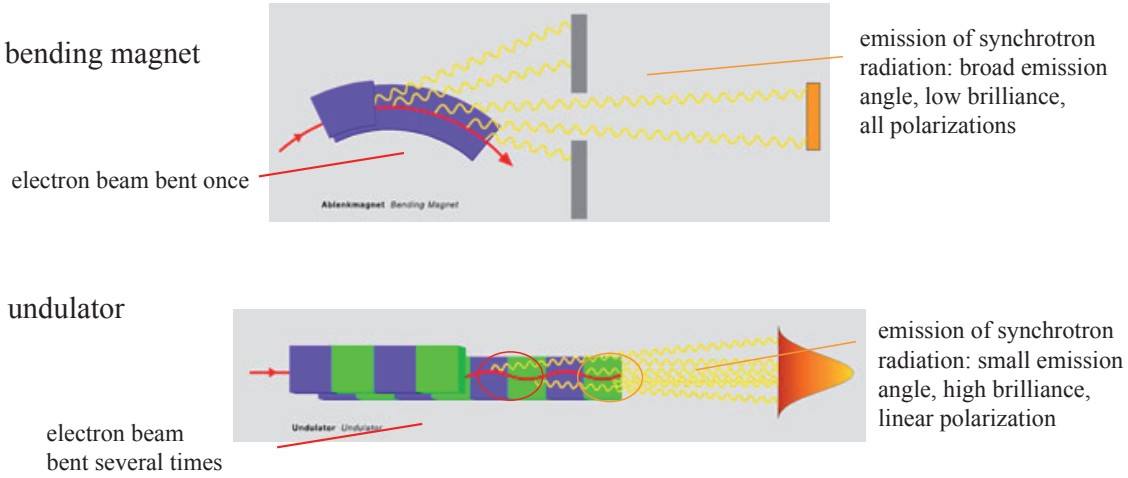

Figure 4.8: *Principles of different insertion devices and their differences [54–56].*

The light emitted from bending magnets and undulators is a continuum light in the wavelength range of 10 eV to 10000 eV for bending magnets and 10 eV to 1500 eV for undulators. This continuum light has to be monochromatized. In both beamlines, shown in figures 4.9 and 4.10, a toroidal mirror $M1$ bundles the divergent emitted snchrotron light in a parallel beam and sends it into the grating chamber of the monochromator. Both beamlines possses a plane grating monochromator (PGM), i.e. the light passes a planar mirror $M2$ onto a planar grating. Mirror and grating are rotated against each other to access the different wavelengths. Leaving the grating chamber the monochromatized light

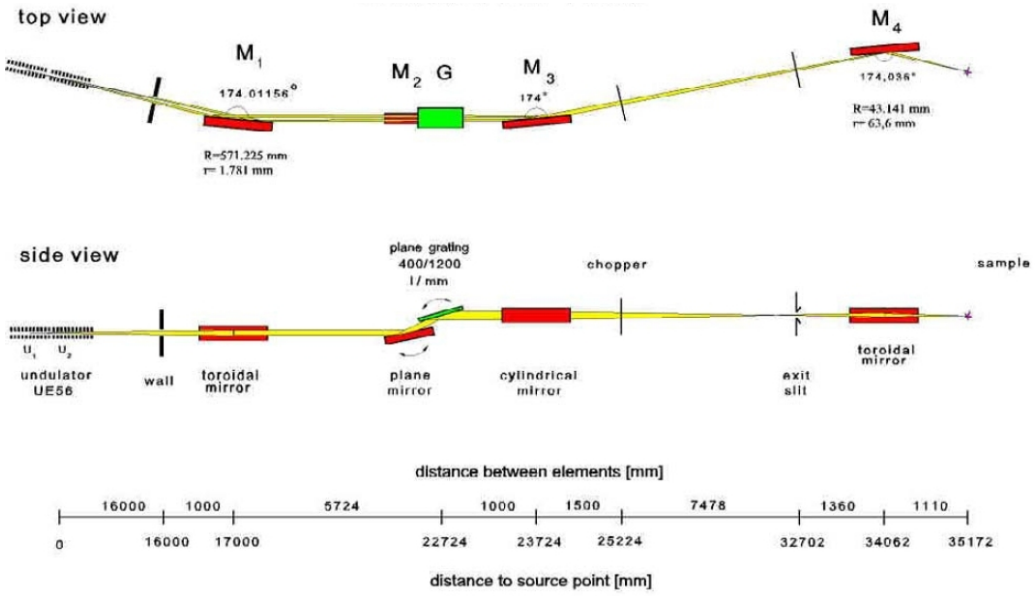

Figure 4.9: *Optical layout of the UE56/2-PGM1 beamline at BESSY. For a detailed description see text. – Figures reproduced from [58].*

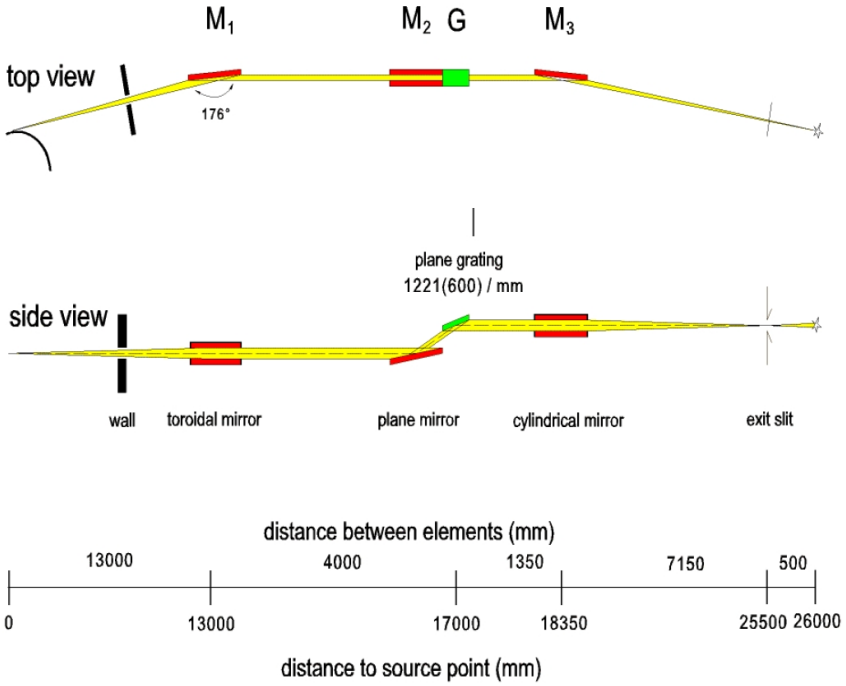

Figure 4.10: *Optical layout of the PM3 beamline at BESSY. For a detailed description see text. – Figures reproduced from [58].*

is refocused onto the beamline focus point in the experimental chamber. In case of the PM3 this is accomplished by one cylindrical mirror $M3$, for the UE56-2 a cylindrical mirror $M3$ and a toroidal mirror $M4$ are used. Directly before the sample (or the $M4$ mirror, respectively) the size of the synchrotron light is limited by the exit slit.

The UE56-2 shows an additional element in the layout. Since the UE56-2 is a double-undulator beamline, i.e. two identical undulators can be coupled producing two beams of synchrotron light (which may e.g. have opposite polarisation). The chopper following $M3$ can be used to selectively block one of the synchrotron beams. In this work the double undulator capability of the UE56/2 has been tested using opposite polarisations for easier C1s-CD measurements. In this work only one undulator (closer to the experiment) was used without the chopper.

While the *UE56/2-PGM1* is an undulator-beamline providing synchrotron light of high flux density, the *PM3* is situated at a bending magnet with considerable lower flux density. This is of importance since organic molecules under investigation here might undergo photon induced decomposition[3], commonly referred to as "beam damage". This has to be constantly monitored throughout the experiments[4] and the flux density of the beamline

[3]Examples are given e.g. in [57].

[4]Monitoring of occurrence of "beam damage" has been performed by close investigation of changes in valence band and core level Spectra.

has to be reduced by choosing a grating with a 1200 lines/mm grating, moving the incoupling mirror $M1$ away from the grating and finally by detuning the undulator position.

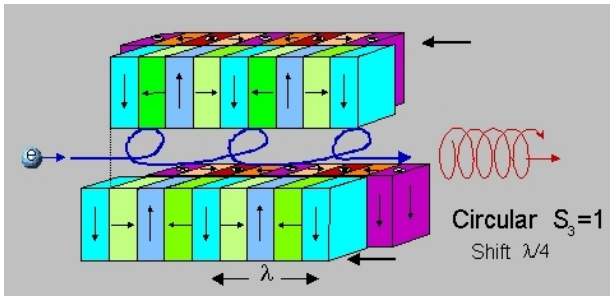

Figure 4.11: *Circular polarisation at the UE56/2 beamline is obtained by lateral shift of the magnet arrays in the undulator[58]. – Figures reproduced from [58].*

The light emitted from a bending magnet in the plane of the electron path is horizontally polarized, while the light emitted above and below the plane is circular polarized, left- and right handed respectively. By adjusting the incoupling mirror M_1 (see figure 4.10) above, in or below the plane light of different polarization can be used. In undulators, electrons are forced on several back-and-forth wiggles. Due to the pairwise arrangement of the magnets, the electrons are deflected only in one plane, creating a beam of linear polarized light. To access circular polarized light, the arrangement of the magnets in the undulator has to be modified. In the case of the *UE56/2*, an "APPLE"-type undulator[59, 60], the direction of magnetization is changed by 90° for every magnet. By changing the alignment of the magnetic arrays towards each other, virtually every polarization can be accessed, as schematically shown in figure 4.11.

To access circular polarized light,here the undulator of the UE56/2-PGM1 was set to a gap of 36.142 mm and a shift of ±19.797 mm resulting in a fully circular polarized light. A positive shift value corresponds to a positive, i.e. right-hand polarisation, determined against propagation direction of the synchrotron light. At the PM3 the incoupling mirror M1 was set to ±0.8 mm for positive and negative circular polarization, respectively[5].

Carbon contamination has also an influence on the rotation angle of circular polarized light, as figure 4.12 shows. Especially close to the carbon adsorption edge around 283 eV and 290 eV photon energy, but also in the range going up to about 330 eV a derivation from the set polarisation can be measured. Figure 4.12 shows the normalised synchrotron light intensity difference $(I_{vert} - I_{hor})/(I_{vert} + I_{hor})$ of horizontal and vertical linear polarised light. In an ideal uncontaminated beamline this value would be zero for all energies. Different absorption of both polarisations through carbon contaminations lead to strong deviations from zero. For circular polarised light used in the experiments here, the same

[5]Due to different definitions positive polarization, which is referred to for experiment, corresponds to negative helicity from the beamline.

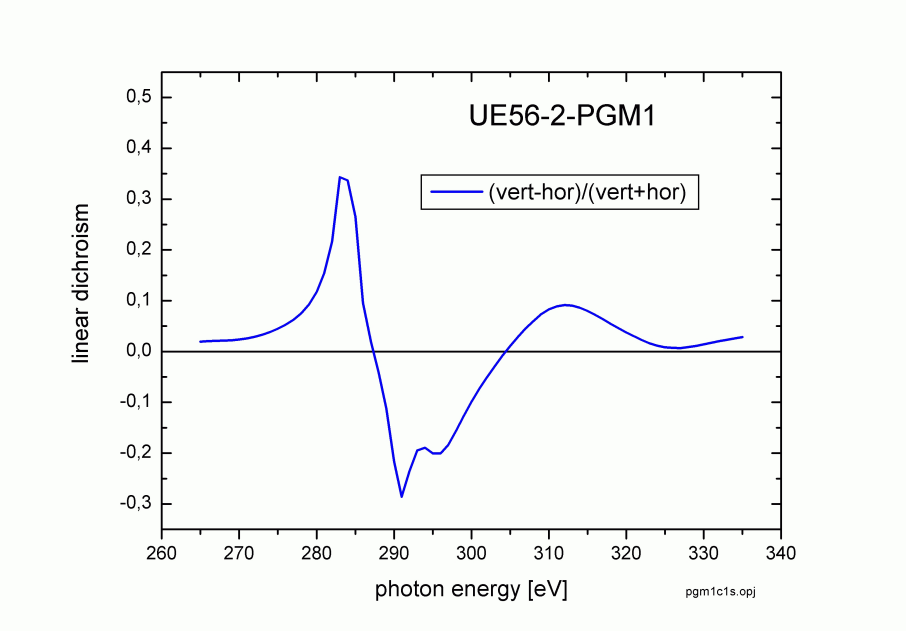

Figure 4.12: *Linear dichroism at the UE56/2-PGM1[61]. The graph displays the normalised intensity difference* $(I_{vert} - I_{hor})/(I_{vert} + I_{hor})$ *of horizontal and vertical linear polarised light. Deviations from the ideal zero-line are due to absorption in carbon contaminations of the beamline.*

behavior can be assumed. To avoid an influence of these contaminations on the C1s-CD investigations, these were mainly performed at 380 eV photon energy.

4.3 Near Edge X-Ray Absorption Fine Structure Spectroscopy (NEXAFS)

Near Edge X-Ray Absorption Fine Structure Spectroscopy (NEXAFS or XANES) is based on the excitation from a K-shell electron, i.e. an electron strongly localised at an atom, into empty states having an enhanced amplitude around the excited atom[62–64] (figures 4.13 and 4.14). These are preferably Rydberg states or antibonding molecular orbitals.

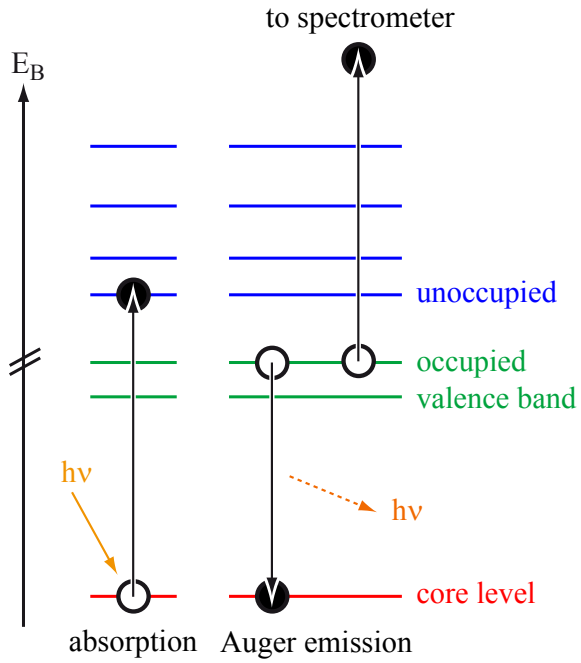

Figure 4.13: *The different steps in NEXAFS. X-rays of varied energy excite electrons from a core level into unoccupied levels. Subsequently an electron from an occupied level fills this hole while an Auger electron is emitted. This is detected by the electron spectrometer. Other detection methods, such as the detection of electron yield, or fluorescence photons, exist.*

For free molecules the situation is rather complex. A spatial overlap of initial and final state has to be fulfilled as well as orientational agreement between exciting light and final state orbital. For adsorbed molecules the situation is slightly simpler[62, 63]. Excitation into several orbitals are symmetrically forbidden. Thus the number of electronic transitions is in principal smaller than for the gas phase. Also excitations take place mostly into orbitals that are not perturbed by the surface interaction, i.e. molecular orbitals incorporated in bonding may not be accessible for excitation. Nevertheless cases may exist, where molecules exhibit the same excitations in gas and in adsorbed phase.

Most of the final states can be identified as antibonding π^* of the the molecular π-system or σ^* orbitals between the molecular backbone, i.e. for hydrocarbons between the C-atoms. But also excitations into hydrogen-derived antibonding states are known[63]. Typically

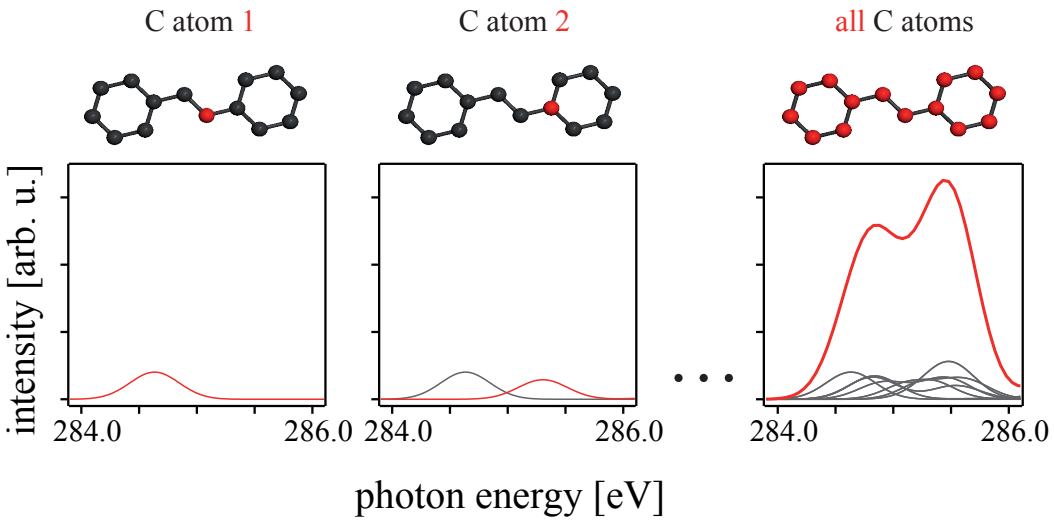

Figure 4.14: *From every C-atom electrons are excited into the unoccupied molecular orbitals. The cross section may vary significantly as the two plots on the left for two exemplary atoms (indicated in red) show. On the right the excitations from every atom as well as the enveloping spectrum is shown. The latter one is the detected NEXAFS spectrum.*

only transitions into the energetically lowest antibonding hydrogen state can be observed. NEXAFS-detection is mostly based on the detection of secondary processes. After electron excitation the generated core hole is subsequently filled with an electron from an upper level. Upon hole decay, either light is emitted or an Auger electron is generated. Either the fluorescence or the Auger electron can be detected. The latter is done in this work.

Normally the π^*-resonance is detected at the lowest energies, below the ionization potential of the molecule[6]. For adsorbed molecules it can be shifted close to the ionization threshold [7] as the final hole is screened quite well. Since for adsorbed molecules the ionization threshold to substrate states is quite close to the π^*-resonance, a steplike background exists in the NEXAFS-spectra (see figure 4.15b). If the sum of atomic numbers Z of multiple-bond atoms in a molecule exceeds 15, as is the case for stilbene with $Z_\Sigma = 84$[8], σ^*-resonances can be found also below the IP, otherwise only within the continuum. The closer to or higher in the continuum theses states are, the higher the probability of a decay into continuum states, leading to a large lifetime broadening of the σ^*-resonances. Also asymmetric vibrational broadening occurs at these resonances for the orbitals that are situated along the vibrating molecular backbone.

For quantitative analysis, NEXAFS spectra have to be normalized and the background

[6] The ionization potential is defined as the binding energy with reference to the vacuum level E_B^V.
[7] The ionization threshold is defined as the binding energy with reference to the Fermi level E_B^F.
[8] $Z_\Sigma = 14$ C-atoms $\times$ atomic number $6 = 84$

has to be subtracted. This has been performed in several steps. In step one, the measured NEXAFS spectra of intensity I were divided by beam intensity measured by the current on the refocussing mirror I_M. Thereby all spectra were normalised on the actual photon flux on the sample. This mirror current is superior to the beam current as normalisation factor, because variations in the beamline, as slight shifts of the mirror positions, alter the actual flux on the sample but are not represented in the beam current, which is only a measure for the number of electrons in the storage ring.

Subsequently, as shown in figure 4.15a a spectrum of the clean sample (also normalised to the mirror current) (dashed red line) is subtracted from the adsorbate NEXAFS spectrum (solid red line), resulting in a NEXAFS spectrum bearing only molecular information (dotted red line). This spectrum (solid blue line in figure 4.15b) still contains the continuum background, described by a stepfunction (dashed blue line). The step I_{step} can best be described by an errorfunction[62, 65] of the type

$$I_{step} = H \cdot \left[\frac{1}{2} + \frac{1}{2} erf\left(\frac{E-P}{W/c}\right)\right] \quad E \leq P + W \ , \tag{4.16}$$

where E is the photon energy (variable), P the position of the inflection point of the step and W the full width at half maximum (FWHM) of the step. The constant c is defined as $c = 2\sqrt{ln2}$. The width W is determined only by the experimental parameters[63]. In this work a width of $W = 1\,\text{eV}$ has proven to be reasonable.

The inflection point P in this work was always located at the energy $P = E_{\pi*-onset} - W$. Therefore the high energy onset $E_{\pi*-onset}$ of the π^*-resonance was determined. As the inflection point was chosen to be exactly the value $W = 1\,\text{eV}$ below this onset, the maximum energy, where equation (4.16) applies is $E = P + W = E_{\pi*-onset}$. Here the step reaches its maximum. At higher photon energies $E > P + W$ an increase of the background can be noticed. Stöhr has shown that this increase is exponential

$$I_{step}^{`} = I_{step} \cdot exp - [d \cdot (E - P - W)] \quad E > P + W \ , \tag{4.17}$$

where d is a decay coefficient. Over the range of a few eV this exponential increase behaves almost linear. As spectra taken in this work normally do not extend beyond 295 eV photon energy, equation 4.17 can be simplified as follows

$$I_{step}^{`} = I_{step} + I_{step} \cdot - [d \cdot (E - P - W)] \quad E > P + W \ . \tag{4.18}$$

The step subtracted spectrum is shown in figure 4.15b as the dotted blue line.

Finally the step subtracted spectrum (solid black line in figure 4.15c) is normalised to the

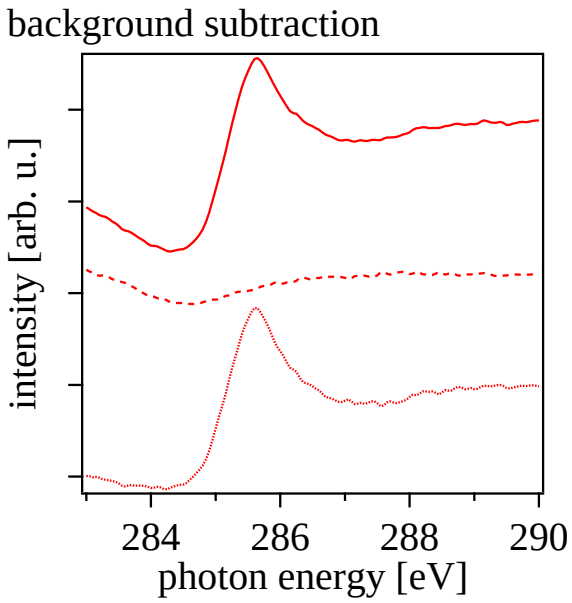

(a) *Subtraction of clean sample.*

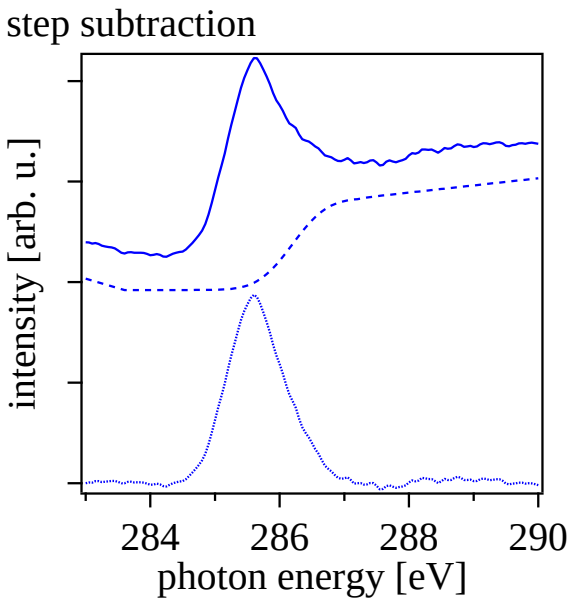

(b) *Step subtraction.*

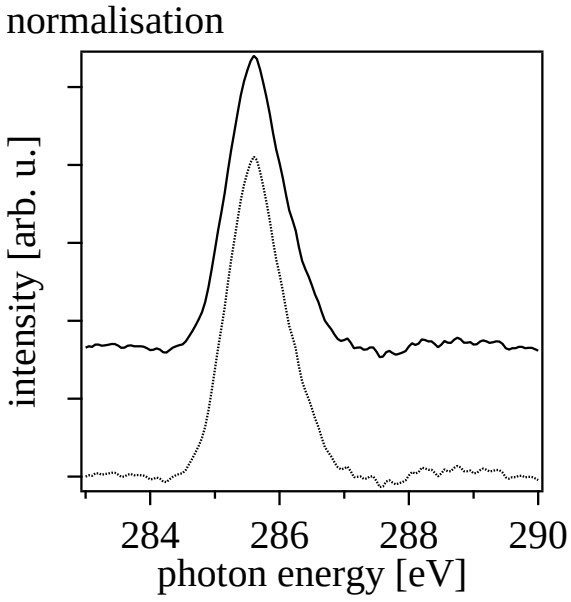

(c) *Normalisation on stepheight.*

Figure 4.15: *Normalisation and background removal of NEXAFS spectra. (a, red) shows the original spectrum (solid line) from which the spectrum of the clean surface (dashed line) is subtracted (dotted line). In (b, blue) from this substrate-subtracted spectrum (solid line) the analytically derived stepfunction (dashed line) is subtracted (dotted line). (c, black) shows the normalization of this (solid line) to the step height, resulting in the final spectrum (dotted line).*

step height H to the spectrum depicted by the dotted black line in figure 4.15c.

The well defined symmetry of the states involved - initial spherical 1s-orbital and final antibonding MOs - leads to a high angular dependence of the NEXAFS spectra. The signal intensity correlates directly with the overlap of the exciting light's E-vector and the final

state orbital. Thereby σ^*- and π^*-orbitals can be distinguished, and the orientation of the molecule on the surface can be determined.

A direct correlation[66] between the NEXAFS resonances and the orbitals as seen by the molecular-orbital (MO) theory[9] exists. Therefore NEXAFS spectra can be directly interpreted by looking at the molecular orbitals, because the resonance intensity is directly determined by the overlap between the E-vector of the exciting light and the so called molecular O-vector. Figure 4.16 shows a simplified scheme of representative σ- and π-orbitals by vectors or planes. The orbital vector O can be seen as the vector pointing along the molecular orbital, i.e. an O_σ- vector points along a bond between two atoms, while an O_π-vector points perpendicular to this bond as the p_z orbitals forming the π-system do. Naturally a molecule does not consist out of only one σ- and one π-bond. Therefore the overall O_σ- and O_π-vectors are a superposition of all σ- and π-bonds. In the case of benzene, where the sigma bonds form a ring with the π-system parallel to it, this results in the vectors shown in figure 4.16. The whole π^*-system is made up from six p_z-orbitals that overlap in the lateral direction but point all parallel in a direction perpendicular to the C-C-bonds. Due to their collinearity they can be represented as a single vector pointing in direction of the p_z-orbitals, i.e. perpendicular to the molecular plane of the phenyl-group. The O_σ vector is a superposition of the vectors ordered ring-like, i.e. a "disk". In the case of stilbene, the aromatic ring is the most appropriate simplification. Figure 4.18 shows the resulting coordinate system. Using Fermis golden rule

$$I \propto |\langle f\,|E \cdot p|\,i\rangle|^2 \ , \tag{4.19}$$

one obtains for a transition from a 1s-state into a molecular orbital's p-state where the orbital can be assumed as a vector, the angular dependence

$$I = Acos^2\delta \ , \tag{4.20}$$

where A is a normalization factor and ´δ the angle between the parallel component of E and O, as shown in figure 4.18. Taking into account the linear polarization of the synchrotron light and the multiple domains, the intensity of the resonance of a vector-orbital is given by

$$I = A\left[1 + \frac{1}{2}\left(3cos^2\theta - 1\right)\left(3cos^2\alpha - 1\right)\right] \ , \tag{4.21}$$

where θ is the light incidence angle of the synchrotron light and α the angle between molecular orbital vector O and the surface normal. Equation 4.21 will subsequently be

[9] An introduction into MO theory can be found e.g. in the book by Reinhold[67].

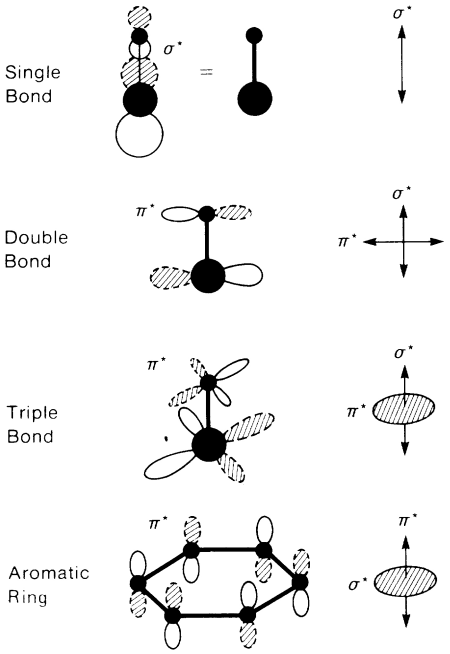

Figure 4.16: *Vectors O representing the molecular orbitals for typical molecular bond classes[63]. The overall vector O is a superposition of every orbital vector at every atom. – Figure reproduced from [63].*

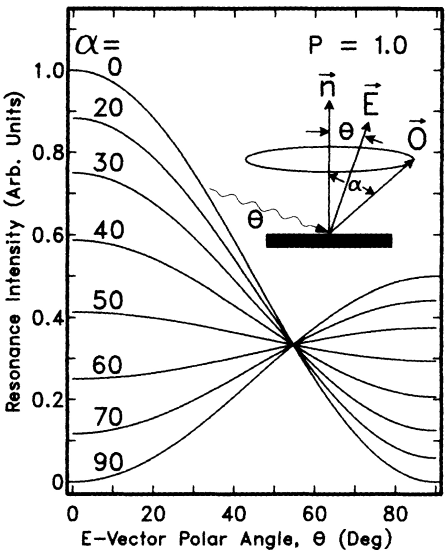

Figure 4.17: *Theoretical resonance intensities for the π*-resonance of an aromatic ring as shown at the bottom of 4.16[63]. At the magic angle of 54.7° there is no angular dependence and the intensity is equal for all α. – Figure reproduced from [63].*

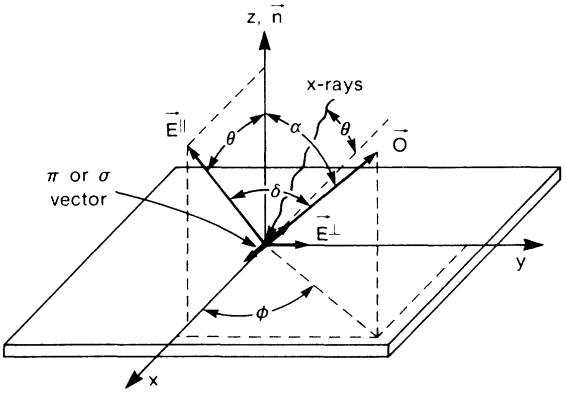

Figure 4.18: *Coordinate system for NEXAFS analysis[63]. x,y and z mark the coordinate system, where z is along the surface normal n and x and y are in the plane. The orbital vector O is displayed with the different angles toward the two E-vectors of the synchrotron light. – Figure reproduced from [63].*

used for all evaluations of angle resolved NEXAFS. Typical intensity behavior for different angles α are shown in figure 4.17. This plot also demonstrates the role of the "magic angle" $\theta = 54.7\,°$[63], which corresponds to "normal emission" in this experiment. Here the NEXAFS spectra do not observe any contribution from the adsorption geometry and the intensity is equal for all tilt angles α. This is straightforward understandable from equation (4.21), as $cos^2(54.7\,°) = 1/3$:

$$I = A\left[1 + \frac{1}{2}\left(3 \cdot \frac{1}{3} - 1\right)\left(3cos^2\alpha - 1\right)\right] \tag{4.22}$$

$$= A\left[1 + \frac{1}{2}\left(1 - 1\right)\left(3cos^2\alpha - 1\right)\right] \tag{4.23}$$

$$= A\left[1 + 0\right] = A\ . \tag{4.24}$$

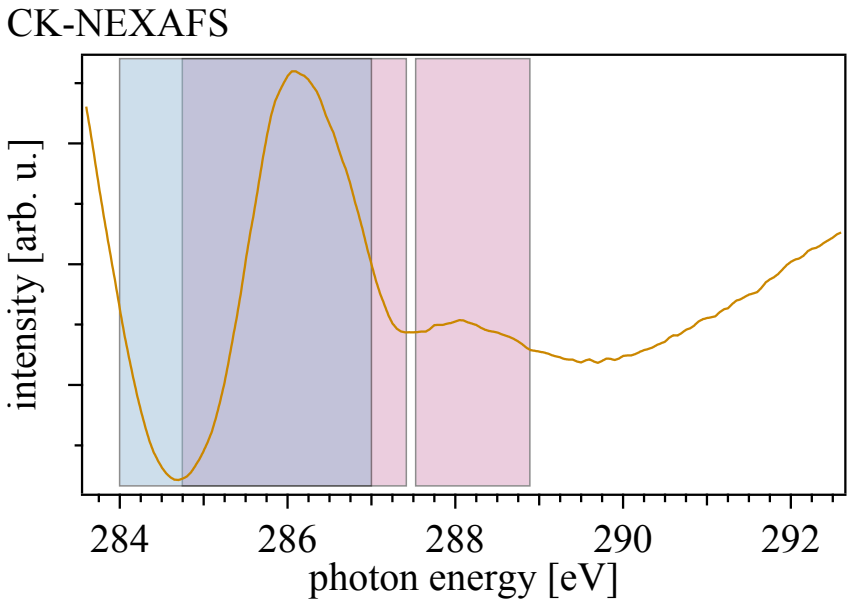

Figure 4.19: *NEXAFS spectrum of a clean Cu(110) surface, normalised to the mirror current, indicating the carbon contamination signal (red) caused by carbon contaminations on the optical elements, and the area of interest (green) in this work.*

The objects of investigation in this work were all organic molecules, i.e. carbon based samples. Therefore mainly the carbon-based spectral features of the samples were inspected. High demands with respect to cleanness of the optical elements are made to the beamlines, since the synchrotron light is otherwise absorbed by carbon-containing contaminations on the optical elements. Unfortunately due to the light weight of carbon containing molecules (e.g. organic molecules but also CO) contamination of the beamlines may easily occur. This can be seen in a typical NEXAFS spectrum from a clean Cu(110) surface, acquired at the UE56/2, in figure 4.19. The areas, where signals from the carbon contamination

occur, are indicated in red. For the experiments in this work, the area between 284 eV and 287 eV was of particular interest, indicated in green. This overlaps directly with the very strong contamination signal with a maximum at around 286 eV. This contamination signal makes the detection of small molecular signals at this energy extremely difficult.

4.4 Scanning Tunneling Microscopy (STM)

Scanning Tunneling Microscopy has been used in this work primarily as an imaging tool. The possibility to utilize the STM for spectroscopy and sample manipulation has not been used[10], and thus the following chapter will focus only on the former aspect.

The Scanning Tunneling Microscope (STM) was first realized by Binnig and Rohrer in 1981[68–70], for this they were awarded the nobel prize in Physics 1986[71]. The idea actually goes back on work by Young and coworkers[72], who were able to establish the fundamental principles underlying the instrument they named "Topografiner". Binnig and Rohrer own the merit of bringing these concepts to work and establish the reliable use of this technique.

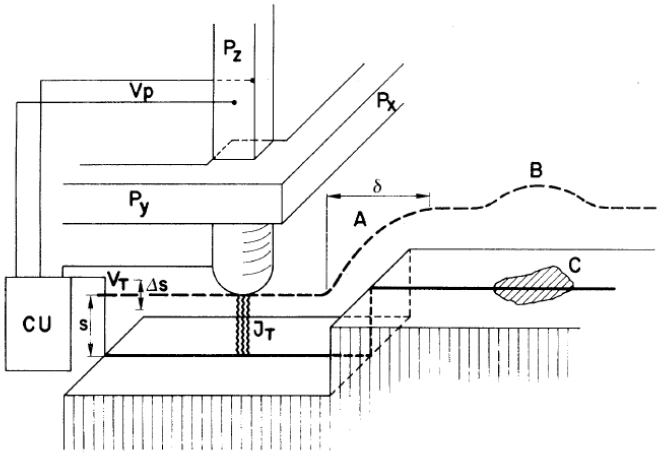

Figure 4.20: *Setup of an STM as described in the original works of Binnig and Rohrer[68, 69]. The piezo dives p_x and p_y scan the tip over the surface. The extension of p_z, whose voltage V_p is controlled by the control unit, is the measure of the surface topography at a constant tunneling current I_T at a given bias voltage V_T. – Figure reproduced from[69].*

In contrast to the variety of deflection and diffraction techniques, which work in the reciprocal space, scanning tunneling microscopy is a technique that allows the imaging of surfaces in "real space". This allows not only for the detection of global structures of long range symmetry, but for the detection of local objects. The results from STM and e.g. LEED can be compared by a Fourier transformation of STM images.

An electrical conducting tip is moved at a small distance over a conductive sample in a raster pattern. Movement is realised by three piezo motors, where two are responsible for the lateral rastering (p_x and p_y), while the main piezo p_z controls the distance of the tip to the sample. As sample and tip are not in direct contact to each other, upon application

[10]Spectroscopy has been performed in a sense that different molecular orbitals of the adsorbate has been imaged as shown in chapter 6.3.1.

of a voltage no current flow can appear in a classical picture. But the STM is based on the fundamental quantum mechanical principle, that electrons can be described either as particles or as waves[73]

$$\phi_0(x) = exp(ik_0x) \tag{4.25}$$

$$k_0^2 = \frac{2m}{\hbar^2}E \ , \tag{4.26}$$

with E being the energy of the electron, $\hbar$ Planck's constant. If these electrons (in the tip) of the STM approach the potential well V_0 of the vacuum between tip and sample, then

$$V(x) = \begin{cases} V_0 > 0 & |x| \leq q_0 \\ 0 & elsewhere \end{cases} , \tag{4.27}$$

where the gap between tip and sample reaches from $-q_0$ to q_0. In the classic description the electrons would be fully reflected

$$\phi_r(x) = \alpha_- exp(-ik_0x) \ . \tag{4.28}$$

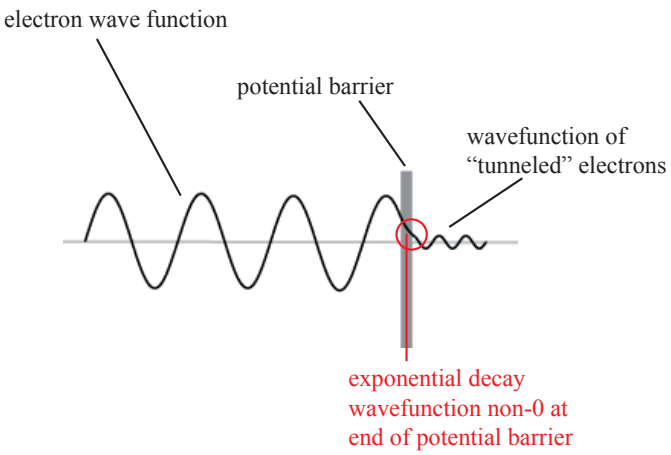

Figure 4.21: *Schematic description of tunneling processes. The approaching electron wave decays exponentially through the potential wall. If the wave has a nonzero amplitude at the end of the barrier, the decreased wave can proceed, the electron has tunneled through the potential wall.*

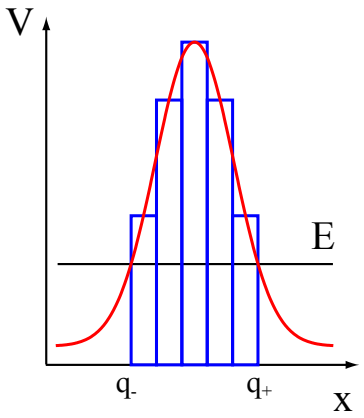

Figure 4.22: *A rectangular barrier as shown in 4.21 is mere theoretical. But any real barrier (red) can be approximated by several rectangular barriers (blue) of different height. Thus the conclusions derived for such rectangular barriers are still valid.*

But in the quantum mechanical picture, the probability distribution $|\phi(x)|^2$ has a solution within the potential well. If $|\phi(x)|^2$ is nonzero at the exit of the well, the electrons may indeed pass the well and travel along on the other side

$$\phi_d(x) = \gamma + exp(ik_0x) \ , \tag{4.29}$$

and thus the total wavefunction is

$$\phi(x) = \begin{cases} \phi_0(x) + \phi_r(x) & -\inf < x \leq -q_0 \\ \beta_+ exp(ikx) + \beta_- exp(ikx) & -q_0 < x < +q_0 \\ \phi_d(x) & +q_0 \leq x < +\inf \end{cases} \ , \tag{4.30}$$

where α_-, $\beta_\pm$ and γ_+ are constants that have to be derived from the boundary conditions. This interplay of reflection and transmission, which can be derived by solution of the Schrödinger equation $H\phi = E\phi$ using above mentioned wavefunction, is described by a transmission coefficient $T(E)$ and a reflection coefficient $R(E)$

$$T(E) = \frac{4x^2}{4x^2 + (1+x^2)^2 sinh^2 2\kappa q_0} \tag{4.31}$$

$$R(E) = \frac{(1+x^2)^2 sinh^2 2\kappa q_0}{4x^2 + (1+x^2)^2 sinh^2 2\kappa q_0} \ , \tag{4.32}$$

where κ is defined as $k = i\kappa$. It is obvious, that $T(E)$ is non-zero at $+q_0$ and thus electrons are able to pass the potential barrier. This process is referred to as "tunneling". In the case of

$$\kappa q_0 = \frac{1}{\hbar}\sqrt{2m(V_0 - E)}q_0 \gg 1 \ , \tag{4.33}$$

the $sinh^2 2\kappa q_0 \approx 1/4 exp(4\kappa q_0)$ term is dominant and $T(E)$ can be simplified to

$$T(E) = \frac{16E(V_0 - E)}{V_0^2} exp(-\frac{4}{\hbar}\sqrt{2m(V_0 - E)}q_0) \ . \tag{4.34}$$

This shows the exponential dependence of the transmission on the width of the potential well $2q_0$ and the effective height $V_0 - E$. These calculations are still based on a rectangular potential well. The real potential well is of course a continuous function. To describe it with the above derived coefficients, it can be approximated by several rectangular potentials, as shown in figure . This figure already indicates, why the tunneling probability strongly increases with increasing E. On the one hand the effective energy $(V_0 - E)$ decreases and

on the other hand the well width $2q_0$.

The tunneling of the electrons through the tip-sample-gap can be measured as a "tunneling current" between tip and sample. Therefore the sample has to be conductive, i.e. a metal or a semiconductor. Insulators may only be used insofar as the insulator layer is thin enough on top of a conductive layer that tunneling occurs through the insulator layer.

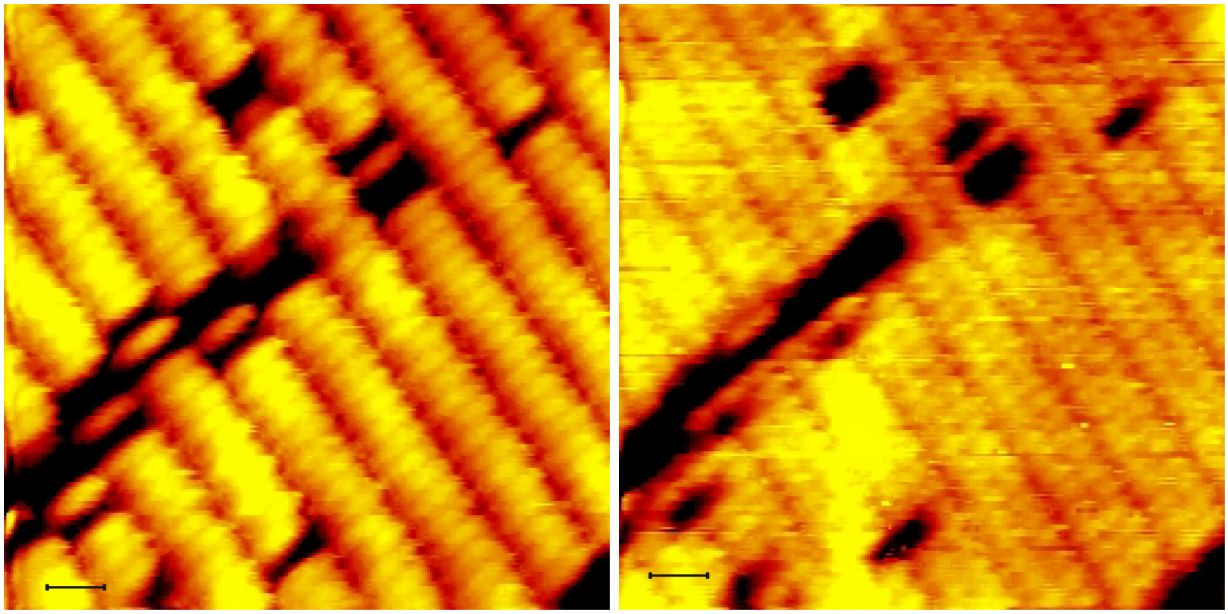

(a) *negative voltage* **(b)** *positive voltage*

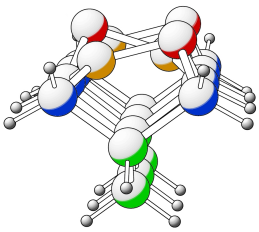

(c) *Si(100)[74]*

Figure 4.23: *The same sample area of a Si(100) is shown in both images. The dimer rows, as depicted in 4.23c are clearly visible in both images. Image 4.23a has been acquired at a negative bias voltage, i.e. electrons tunneling from the occupied orbitals between the dimer atoms into the tip. Image 4.23b has been acquired at a positive bias voltage, i.e. electrons tunneling from the tip into the unoccupied orbitals located at each dimer atom. ((a): -1.68 V, -0.240 nA, 1 nm scale; (b): +1.68 V, +0.260 nA, 1 nm scale)*

The tunneling current directly depends on the width of the gap between tip and sample, as equation (4.34) shows. This is only in the first approximation the distance between tip and surface topography, but, more precisely, the distance between the tip and the electron cloud of the surface orbitals. Thus STM is a method to image the electronic structure of the surface.

Two basic operation modes for an STM exist, which differ in the parameter kept constant and the parameter varied. In the "constant height modus" the absolute height of the tip above the sample is kept constant. With the varying topography of the sample the tunnel current changes which can be used for reconstruction of the actual sample topography. On steep samples the risk of tip-crashing exists in this mode, but very high scanning speeds may be realized. For the "constant current mode" the tunneling current is to be kept constant, therefore the absolute tip-height has to be varied and readjusted for every data point to keep the current constant. This change in absolute height is a direct measure for the sample topography. This mode has solely been used throughout this work.

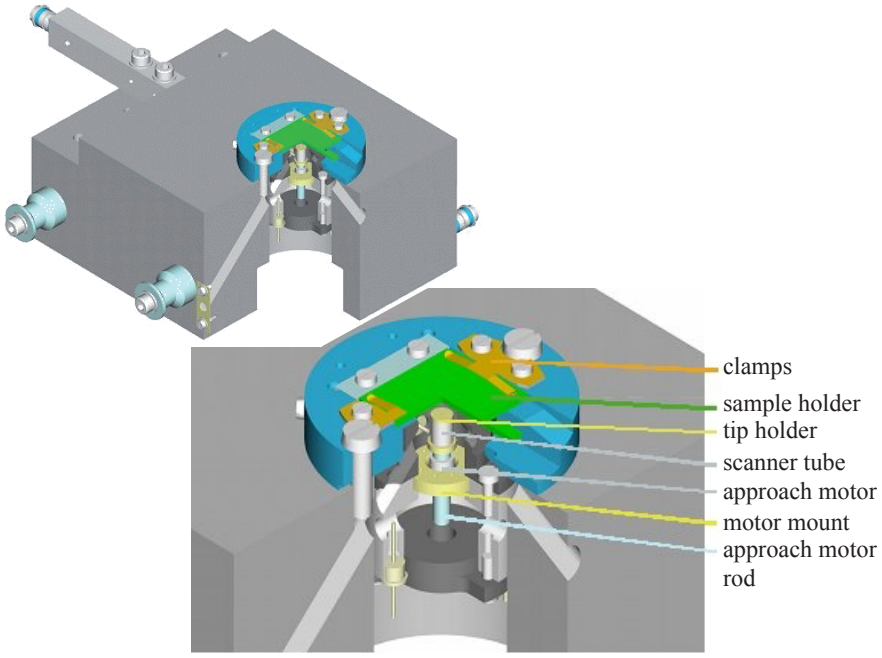

Figure 4.24: *Scheme of the SPECS VT-STM used in this work.*

Equation (4.34) does not only contain the dependence of the tunneling current on the gap width but also on the effective potential. Thus by varying E, the applied potential between tip and sample, the tunneling current changes. As mentioned before, tunneling takes place between the tip and the different surface orbitals. These are, of course, at different energies , these might be bonding and antibonding, occupied or unoccupied orbitals. With the change of the amplitude of the applied voltage, the possibility of tunneling into different orbitals of higher or lower energy is changed. In certain cases the visualization of different orbitals is possible, as Repp and coworkers have only recently demonstrated[75]. Depending on the sign of the applied voltage it is possible to tunnel either from the tip into unoccupied orbitals (negative voltage at the tip) or from the occupied orbitals into the tip (positive voltage at the tip). This is nicely demonstrated by the two images of Si(100) in figure 4.23. There the dimer rows, as depicted in 4.23c are imaged at negative (figure

4.23a) and positive (figure 4.23b) bias voltages. For negative bias voltage the electrons tunnel from the occupied orbitals between the dimer atoms into the tip. At positive bias voltages the electrons tunnel from the tip into the unoccupied orbitals located at each dimer atom.

Here an Aarhus type STM which is based on the STM developed by Besenbacher and coworkers[76]. The main approach is here realized by an inchworm mechanism shown in figure 4.24, i.e. a piezo tube with three clamps. Movement is realized by the contraction and extension of the piezo with the upper and lower clamp holding in alternation. This allows for very rapid tip approach. Vibration damping of the STM, which is held by three springs, is achieved by two viton rings attached. Together with three pressurized-air feet damping the chamber, excellent damping was possible and atomic resolution easy to achieve. The STM can be cooled to about 150 K by means of liquid nitrogen flow cooling. One single tungsten tip was used for all experiments, self etched with KOH solution and subsequent electron bombardment cleaning from a filament located directly on a sample holder.

4.5 Photoisomerisation (UV lamp)

For UV-exposure of samples a mercury arc lamp LOT-Oriel 66033 powered by a LOT-Oriel 68810 power supply and equipped with a monochromator LOT-ORIEL model 7240 has been used. The arc lamp and monochromator were mounted outside the chamber, light was fed into the chamber through a sapphire window. For UV-light in the wavelength range between unit[250]nm and 450 nm these windows have about 85% transmission. For several wavelengths, the output from the monochromator has been tested with a spectrometer. The exemplary spectrum at 365 nm wavelength is shown in figure 4.25a. A gaussian profile was used to fit the data points. Actual output of 371.35 nm wavelength could be determined with a linewidth of below 5 nm. The offset of about 6 nm between set and actually emitted wavelength was confirmed for all tested wavelengths. It can thus be treated as a systematic experimental error. Throughout this work, the set wavelength will be given. For higher wavelengths the linewidth does not broaden significantly. But at around unit[450]nm the appearance of higher harmonic transmission through the monochromator has been observed.

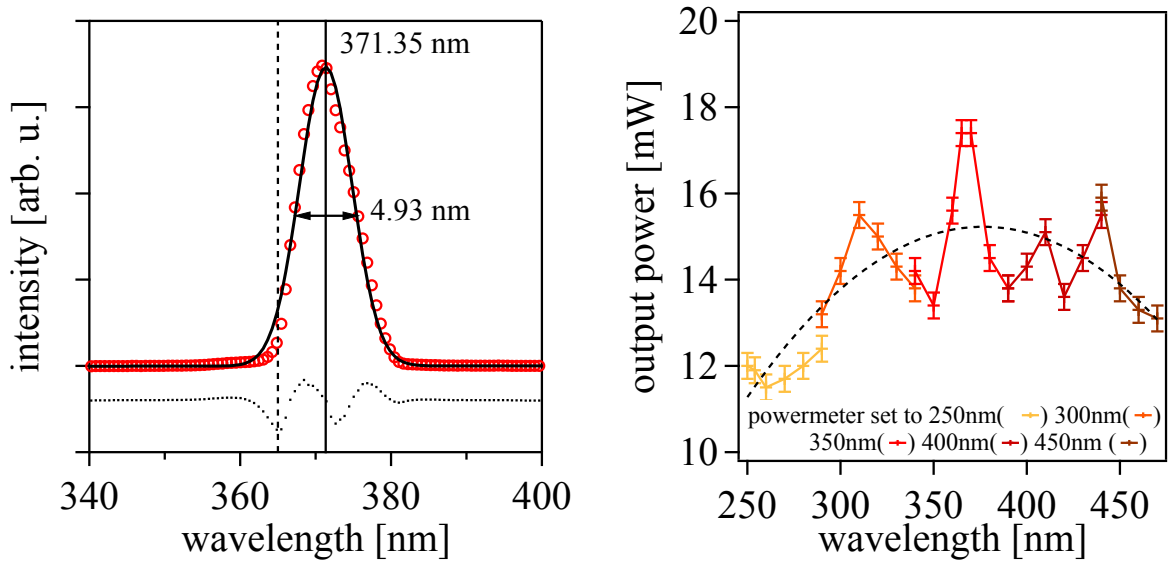

(a) *spectrum* **(b)** *power*

Figure 4.25: *(a) Exemplary spectrum of UV-emission at 365 nm wavelength set at the monochromator (dashed line). The resulting light has its maximum at 371.35 nm and a width of 4.93 nm. (b) Power output of the UV-Arc-Lamp with monochromator for the used wavelength range.*

For exposure the lamp was focused onto the sample utilizing visible (green) light. A sample covered with phosphor-based fluorescence material[11] was used to determine the

[11] `http://www.honeywell.com/sites/sm/lumilux/de/`

actual focal spot for UV wavelengths. No significant perturbation of the focus determined with visible light could be detected.

For the applied wavelength range the Arc lamp had an output power of 14 mW average (figure 4.25b).

Two different exposure modes were used throughout this work:

- Discrete exposure of the sample at one particular wavelength, mostly 365 nm (371 nm systematic error corrected), for a longer timescale of 30 min to 90 min. After each UV exposure photoemission spectra were recorded to control for possible dissociation of the molecules. NEXAFS spectra were recorded to monitor the state of isomerisation.
- Cumulative exposure of the sample to a broad wavelength range, mostly 250 nm to 450 nm (corrected 261 nm to 461 nm). Wavelength was changed by 10 nm every 3 min. XPS/UPS and NEXAFS spectra were only recorded after completion of the whole exposure cycle.

4.6 Theoretical Calculations

For a better understanding, the results obtained by photoemission and especially by NEXAFS have been supplemented by theoretical calculations.

All theoretical calculations in chemistry and physics aim for the complete and thorough description of the ground state of a system, which can then be used to determine the systems characteristics and behavior. Density functional theory[77] is based on the Hohenberg-Kohn-theorems, stating that for every system with N electrons there exists a one-to-one relationship between the ground state spatially dependent electron density $n(\vec{r})$ and the ground state wavefunction[78]. If this electron density can be determined, principally all properties of the system can be deduced from that, i.e. all properties are functionals of the density. The second theorem proves that the total electronic energy is minimized by this ground state density.

Traditional theoretical approaches, the most well known in chemistry being Hartree-Fock theory[67], are based on the exact description of the ground state by a many-body wave function. This wavefunction is dependent on three spatial variables for each of the N electrons, so $3N$ variables in total. The density used in DFT on the other hand is only dependent on the three spatial variables and thus much easier to solve.

The basic quantum mechanical formula is the Schrödinger equation

$$H\Psi = E\Psi \ , \tag{4.35}$$

where H has contributions describing the kinetic energy of every electron, the electron-electron interactions, the electron-nuclei interactions, and the movement of the nuclei. The nuclei are so much larger in mass and their movement is in comparison so much slower then that of the electrons, such as in a first approximation the nuclei can be assumed stationary. This is the so-called Born-Oppenheimer approximation. Therefore only the interaction of the electrons in a static potential has to be described

$$H = -\frac{1}{2}\sum_{i=1}^{N}\nabla_i^2 + sum_{i<j}\frac{1}{|r_i - r_j|} + \sum_{i=1}^{N}V(R_i) = T + U + V \ , \tag{4.36}$$

where the first part is the kinetic energy, the second part the electron-electron Coulomb interaction and the third part the external local one-electron potential. This term still contains interactions between every particle. Kohn and Sham simplified this equation by approximating this system by a system of non-interacting particles in a so called effective potential[79], thus reducing the equation to a single-particle equation T_S plus an additional exchange term correcting the single particle solution for the correct many-particle solution

V_S with $n_S(\vec{r}) = n(\vec{r})$

$$H = T_S + V_S \tag{4.37}$$

$$V_S = V + U + (T - T_S) \ . \tag{4.38}$$

The term $T - T_S$ can be expressed by an exchange-correlation potential V_{XC} including all many-particle interactions. As this contribution is unknown, it has to be guessed. With the initial guess the Schrödinger equation is solved, the wavefunction determined and that is used for a new calculation of V_{XC}. This process is repeated until the results are self-consistent.

From the calculated electron density not only the molecular orbitals can be derived but also the relative charge distribution around the atom nuclei.

The major challenge thereby is to find a good approximation for V_{XC} to start. A commonly used approach is the local-density approximation, where the functionals depend only on the electron density at the coordinate the functional is evaluated at, i.e. $V_{XC} = V_{XC}(n(r))$. This approach is extended by the introduction of gradient corrections, so that the functionals do not only depend on the density but also on the change of the density. For this generalized gradient approximation (GGA) $V_{XC} = V_{XC}(n(r), \nabla n(r))$. A wide range of functionals exist, which are commonly denoted by the first characters of the developers' names. One of the most common functionals is the B3LYP functional, that has been developed by Becke[80], Lee, Yang and Parr[81], where the approximated exchange energy is combined with exact Hartree-Fock (HF) results.

$$V_{XC}^{B3LYP} = V_{XC}^{LDA} + a_0(E_X^{HF} - E_X^{LDA}) + a_X(E_X^{GGA} - E_X^{LDA}) + a_C(E_C^{GGA} - E_C^{LDA}) \ , \tag{4.39}$$

where $_{XC}$ denotes exchange-correlation, $_X$ and $_C$ exchange and correlation, respectively. LDA,GGA and HF denote the different methods as mentioned above. The values for the a-factors are: $a_0 = 0.20$, $a_X = 0.72$ and $a_C = 0.81$[82].

Depending on the complexity and accuracy needed of a DFT calculation the complexity of the functions used to describe the molecular orbitals can be varied. These sets of functions are called "basis sets". Minimal basis sets, denoted as $STO - nG$ (N an integer) use n primitive gaussian functions. The coefficients used to describe the different atoms have been derived by least-squares fitting of *S*later-*t*ype atom *o*rbitals (STO). More advanced basis sets provide a multiple of functions for each orbital. These are called split-valence

basis sets. Split-valence sets from the group of Pople have the notation $XY-Zg$, where X describes the number of primitive gaussians describing each core orbital and Y and Z the number of basis sets used for the valence orbitals split in two. Also splits in three or more parts is possible, the numbering is extended likewise. The basis sets developed by Dunning and coworkers are denoted as follows: $cc-pVNZ$, where $cc-p$ stands for correlation consistent polarized, the V indicates their validity only for valence bands, and N denotes the splitting in N bases.

For calculation of molecular orbitals I used mainly the Gaussian[83] software package, which is based on the work of John Pople[77, 84]. Here the B3LYP functional mentioned before was utilized to determine the ground state of single entities of the molecules under investigation. Beforehand all molecules were geometry optimized, i.e. the Kohn-Sham energy was optimized depending on the coordinates of the nuclei. From the ground state the charge distribution at the nuclei, the molecular orbitals and their binding energies were determined using a $6-31g$ basis set. The results were used to provide a base for qualitative comparison to the measured spectra. As will be shown later, these calculations provided some good indications for the interpretation of valence band and NEXAFS spectra. For visualization of the results obtained with Gaussian the program, Gaussview[85] and JMolEditor[86] were used.

The calculations aiding the NEXAFS interpretation have been performed in close cooperation by Christine Kolczewski from the theory department in the FHI. A different software package has been used, the StoBe-package[87], which is a modified version of the DFT-LCGTO program package DeMon[88], originally developed by A. St.-Amant and D. Salahub, with extensions by L. G. M. Pettersson and K. Hermann. The StoBe-package is specialized for the calculation of absorption spectra. It uses Kohn-Sham orbitals based on a localized basis, i.e. gaussian type orbitals (GTO). The functionals are gradient corrected. What is specific for StoBe is that a double-basis set is used. While a normal basis is used for the initial electron density, a very large diffuse basis set is used in a second step to describe the excited electrons. The first basis set, the "orbital basis", are atom-optimized gaussian functions, that are extended by functions describing the polarization, the diffuse and correlation within the molecule. The latter one, the "auxiliary basis" is an exchange-correlation basis containing high-exponent s-type functions and low-exponent s,p,d-type functions.

For the determination of the excited state, an electron is removed from from every atom into an unoccupied state. In this way all possible transitions from every atom into every unoccupied state are calculated and their transition cross section determined. These values are convoluted with a gaussian to result in the absorption spectra. The gaussian usually has a width of 0.3 eV up to the ionisation potential of the atoms and subsequently increases over the next 10 eV up to 4.5 eV. It has to be remarked that the thus-determined

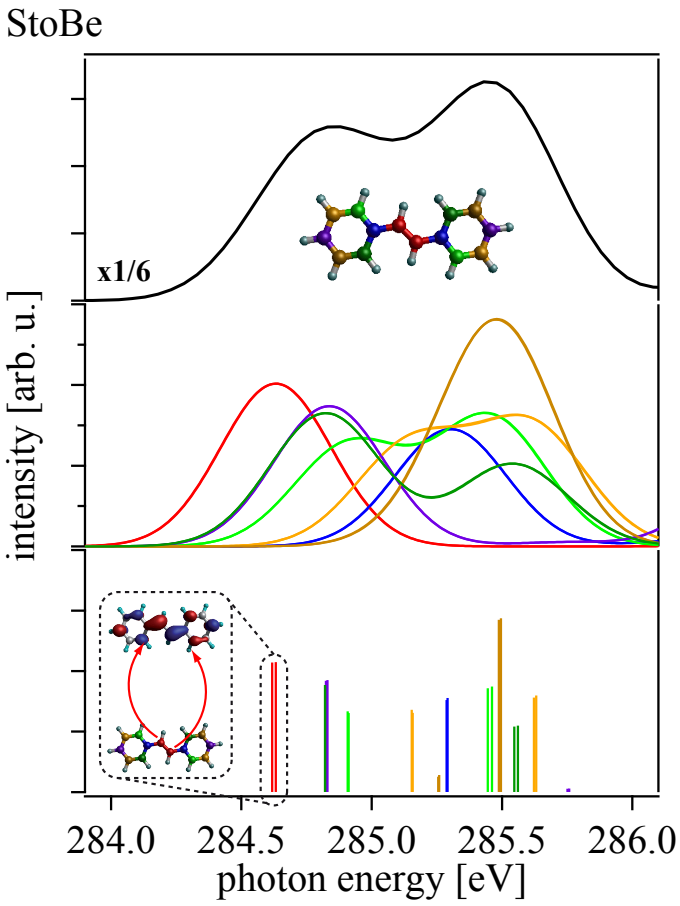

Figure 4.26: *The coloured lines (bottom) show the strength of the transition cross section of transitions from the CK-shell of every atom into the unoccupied molecular orbitals. The emission from one atom is coded through one color as shown in the inset. The different excitation energies correspond to excitations into different unoccupied orbitals. Convolution with a gaussian of 0.5 eV width results in the single-atom spectra shown in the middle. A superposition of all these spectra gives the envelope function in the top part. This is the actual NEXAFS spectrum that can be compared to the experimental data.*

spectra always have to undergo a subsequent correction for the ionization potential, which corresponds to a small shift in total energy.

Though StoBe is specialized to absorption spectra calculations, two limitations exist. First, the number of atoms in the cluster is rather limited with 60 atoms in the Windows version. Thus large surface assemblies cannot be realized and the influence of e.g. neighboring molecules on a surface is not included in the calculations. Secondly, the actual cross section, lifetime and decay-paths of the excited states in molecules are not so well described. Also here the influence of surfaces on these parameters is not included in the calculations. How strong the drawback due to these limitations is, can be seen in the following chapters.

4.7 Samples and Preparation

4.7.1 Si(100)

The silicon samples used were approximately 0.3 mm by .0]mm in size, cut from a p-doped[12] Si(100)-wafer from Virginia Semiconductor[13] and mounted on the sample holder in a half-isolated fashion allowing application of a current through the Si(100) slab. Sample cleaning was performed by applying direct current heating. The slabs were flashed to 1200 °C, cooled down quickly to about 900 °C for five seconds and then postannealed at 0.5 A for another five minutes[89]. The flashing temperature was checked with a pyrometer. This preparation cycle initially had to be repeated about three times. For the coverages usually used throughout this work, one flashing and annealing cycle was already sufficient for proper cleaning. Cleanness of the sample was checked by LEED and XPS.

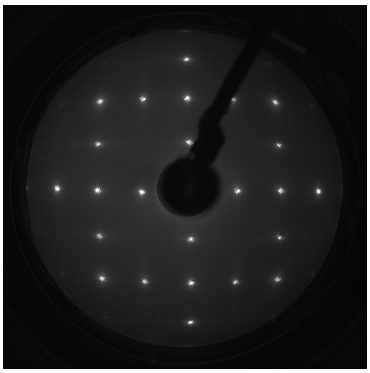

Figure 4.27: *Si(100). Exemplary* 2×1 *spectrum obtained for a freshly cleaned Si(100) surface at 96 eV electron kinetic energy.*

4.7.2 Cu(110)

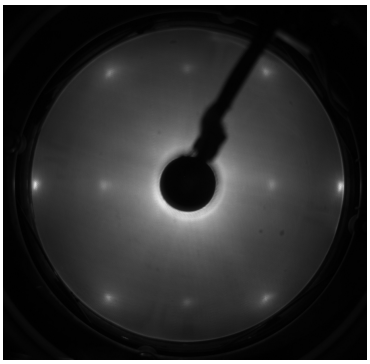

Figure 4.28: *Cu(110). Exemplary spectrum obtained for a Cu(110) surface posterior to ion bombardment and annealing at 120 eV electron kinetic energy.*

The copper sample was directly mounted to a sample holder. Sample cleaning was performed through ion bombardment and annealing. Therefore the Cu(110) sample was bombarded by argon ions accelerated to $1.5kV$ and a filament current of $35mA$. The resulting sample current was around $3\mu A$. Ion bombardment was performed for 15 minutes. Simultaneously the crystal was heated via electron bombardment through a filament operated at $3.3V$ and $1.6A$. Annealing was continued after bombardment for another 15 minutes at the same parameters. After initial cleaning at the beginning of a beamtime, usually one ion-bombardment-and-annealing-cycle was sufficient for proper cleaning of the sample after an adsorption experiment. Cleanness of the sample was checked by LEED and XPS.

[12] Boron-doped, resistivity 7.5 $\Omega cm to 12.5\,\Omega$cm

[13] `http://www.virginiasemi.com/`

4.7.3 Adsorbates

Stilbene

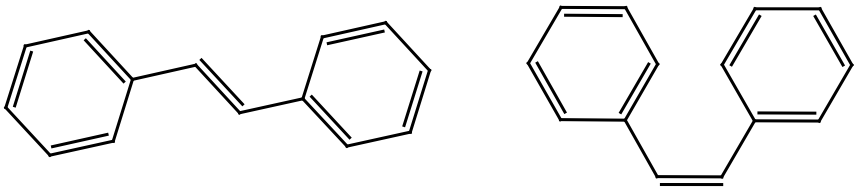

Figure 4.29: *Stilbene*

Stilbene (SigmaAldrich, order nos. 139939 and S4808 for trans- and cis-Stilbene respectively) was used without further purification. Both isomers were evaporated from a glass tube, in the case of trans-stilbene heated to $90°C$, through a leak-valve. The difference in evaporation temperature correlates with the higher boiling point of trans-stilbene under standard conditions. Exposures were determined by means of pressure times exposure time[14]. In this work a monolayer coverage is defined as the saturation coverage at room temperature, which is reached after an exposure of $3L$ on Si(100) and $7L$ on Cu(110).

4,4'-Stilbene-dicarboxylic acid

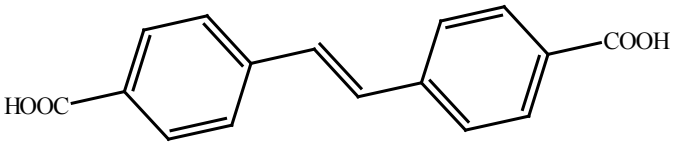

Figure 4.30: *4,4'-Stilbene-dicarboxylic acid*

4,4'-Stilbene-dicarboxylic acid (Alfa Aesar, order no. A11839) was used without further purification. It was evaporated from a Knudsen type cell at temperatures between $453K$ and $488K$. Depending on the substrate temperature different phases with specific surface reconstructions could be obtained.

[14]Langmuir: $1L = 1\Delta 10^{-5} Torrs$

Tartaric Acid

Tartaric Acid (Sigma-Aldrich, order nos. F95320 and F95308 for D- and L-Tartaric Acid respectively; Acros, order no. 137875000 for m-tartaric-Acid) was used without further purification. All isomers were evaporated from a Knudsen-type oven through a gate valve at temperatures of around $115°C$. Depending on substrate temperature and deposition time, different coverages and phases with specific surface reconstructions could be obtained.

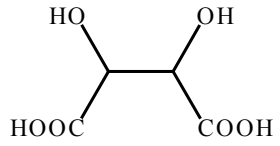

Figure 4.31: *Tartaric acid*

Alanine

Alanine (Sigma-Aldrich, order nos. F05140 and F05129 for D- and L-Alanine respectively) was used without further purification. All isomers were evaporated from a heated glass tube through a gate valve at temperatures of around $100°C$ for $1200s$ onto the Cu-substrate kept at $330K$. Thus the $(2\ \pm 2|\mp 5\ 3)$-phase could be reproducibly prepared.

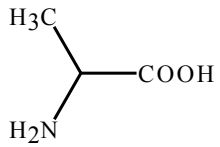

Figure 4.32: *Alanine*

Cysteine

Cysteine (Sigma-Aldrich, order nos. F30095 and F30089 for D- and L-Cysteine respectively) was used without further purification. All isomers were evaporated from a heated glass tube through a gate valve at temperatures of around $115°C$ onto the Cu substrate kept at $335 - 340K$. In order to obtain the $(4\ \mp 1|\pm 1\ 5)$-phase an initial "seeding" evaporation for about $10s$ had to be followed by a second evaporation of $30s$ duration. Sole evaporation of $40s$ time led only to a disordered phase.

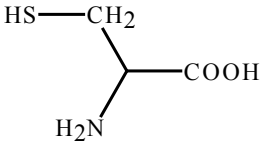

Figure 4.33: *Cysteine*